Short article

Developmental Cell

# Cellular damage triggers mechano-chemical control of cell wall dynamics and patterned cell divisions in plant healing

## Graphical abstract

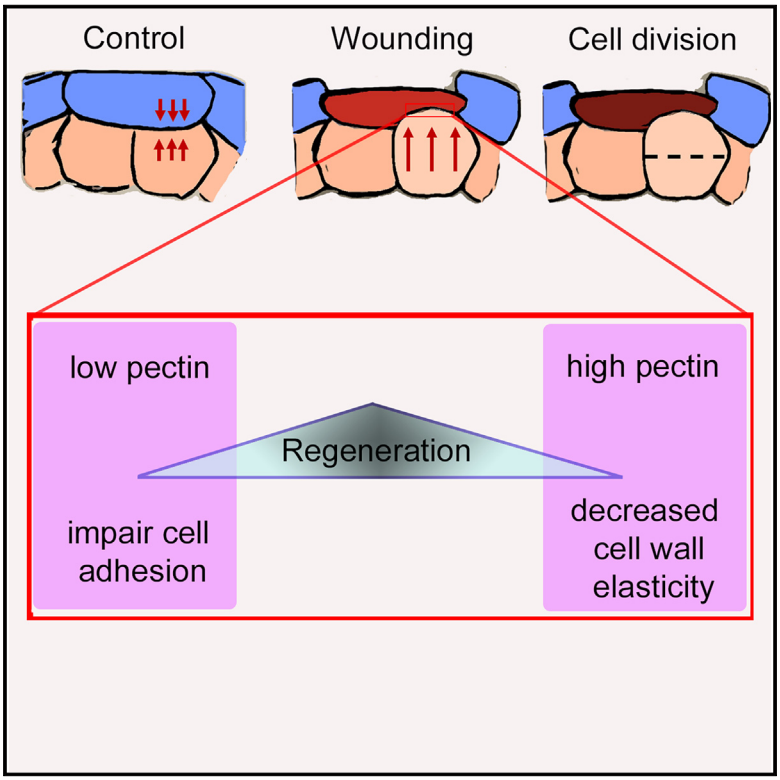


## Authors

Luciano Martín Di Fino, Muhammad Shahzad Anjam, Maarten Besten, ..., Panagiotis N. Moschou, Richard S. Smith, Peter Marhavý

## Correspondence

peter.marhavy@slu.se

## In brief

Di Fino et al. analyzed the biomechanical properties of the cell wall in the *Arabidopsis* root and found that xylem pole pericyclic cell walls are more flexible than outer cell walls. This flexibility enhances their ability to sense mechanical stimuli and activates regeneration responses, aiding tissue repair and damage mitigation.

## Highlights

- Cell wall composition controls *Arabidopsis* root regeneration
- Xylem pole pericycle displays distinct mechanical properties
- Xylem pole pericycle cells initiate regeneration in response to mechanical stimuli
- Ethylene controls cell wall properties to influence the regeneration response

Di Fino et al., 2025, Developmental Cell *60*, 1411–1422
May 19, 2025 
https://doi.org/10.1016/j.devcel.2024.12.032

CellPress

Developmental Cell

CellPress
OPEN ACCESS

Short article

# Cellular damage triggers mechano-chemical control of cell wall dynamics and patterned cell divisions in plant healing

Luciano Martín Di Fino,[1] Muhammad Shahzad Anjam,[1] Maarten Besten,[2] Andriani Mentzelopoulou,[1,3] Vassilis Papadakis,[4,5] Nageena Zahid,[1] Luis Alonso Baez,[6] Nicola Trozzi,[7] Mateusz Majda,[7,9] Xuemin Ma,[1] Thorsten Hamann,[6] Joris Sprakel,[2] Panagiotis N. Moschou,[3,5,8] Richard S. Smith,[7] and Peter Marhavý[1,10,*]

[1]Umeå Plant Science Centre (UPSC), Department of Forest Genetics and Plant Physiology, Swedish University of Agricultural Sciences, 901 83 Umeå, Sweden
[2]Laboratory of Biochemistry, Wageningen University and Research, Stippeneng 4, 6708 WE, Wageningen, the Netherlands
[3]Department of Biology, University of Crete, Heraklion, Greece
[4]Department of Industrial Design and Production Engineering, University of West Attica, 12244 Athens, Greece
[5]Institute of Molecular Biology and Biotechnology, Foundation for Research and Technology-Hellas, Heraklion, Greece
[6]Institute for Biology, Faculty of Natural Sciences, Norwegian University of Science and Technology, 5 Høgskoleringen, 7491 Trondheim, Norway
[7]Department of Computational and Systems Biology, John Innes Centre, Norwich NR4 7UH, UK
[8]Department of Molecular Sciences, Uppsala BioCenter, Swedish University of Agricultural Sciences and Linnean Center for Plant Biology, Uppsala, Sweden
[9]Present address: Department of Plant Molecular Biology, University of Lausanne, 1015 Lausanne, Switzerland
[10]Lead contact
*Correspondence: peter.marhavy@slu.se
https://doi.org/10.1016/j.devcel.2024.12.032

## SUMMARY

Reactivation of cell division is crucial for the regeneration of damaged tissues, which is a fundamental process across all multicellular organisms. However, the mechanisms underlying the activation of cell division in plants during regeneration remain poorly understood. Here, we show that single-cell endodermal ablation generates a transient change in the local mechanical pressure on neighboring pericycle cells to activate patterned cell division that is crucial for tissue regeneration in *Arabidopsis* roots. Moreover, we provide strong evidence that this process relies on the phytohormone ethylene. Thus, our results highlight a previously unrecognized role of mechano-chemical control in patterned cell division during regeneration in plants.

## INTRODUCTION

The development of multicellular organisms is regulated by a combination of chemical, molecular, and physical signals that contribute to tissue and organ morphogenesis.[1,2] The responses of individual cells to developmental signals can also impact the growth and behavior of neighboring cells through distinct feedback mechanisms.[3,4] Dynamic rearrangements in the microtubule cytoskeleton of a plant cell and modulations in hormone transporters following mechanical stress influence cell wall (CW) synthesis and cell expansion.[5] These changes, together with alterations in cell shape, establish a feedback loop in which stress patterns cooperatively regulate cell growth and tissue form. This feedback process is involved in the maintenance of ''tensegrity'' balance, which describes the mechanical stability of a CW based on the balance between tension and compression. Ultimately, this tensegrity balance has significant implications for developmental processes in plants.[6] This makes it clear that the interplay between cells and the surrounding environment, along with recursive feedback, is a fundamental aspect of both plant and animal development.[6] In the plant root, various cell layers can be subjected to distinct mechanical stress from neighboring cells.[7] Therefore, extensive research has focused on identifying the plant cell mechanisms that enable the perception of, as well as response to, mechanical stress.[8,9] Mechanical CW damage can trigger the activation of molecular signaling pathways, which subsequently stimulate a series of cellular events with the purpose of repairing the damaged CW and restoring integrity.[10–12] CW mechanical properties are particularly important during wound healing and defense against pathogen invasion, as these properties determine whether the CW will be able to withstand mechanical pressure.[8,9,13] Following wounding, the CW can be reinforced through the incorporation of additional layers of structural components, such as cellulose and lignin.[13] Moreover, CW composition influences various CW properties, e.g., elasticity and viscoelasticity, all of which strongly affect cell growth and expansion.[14–17]

Recent studies have identified that mechanical properties, including elasticity, influence the perception and transduction of mechanical signals in the CW.[9,18] These mechanical signals,

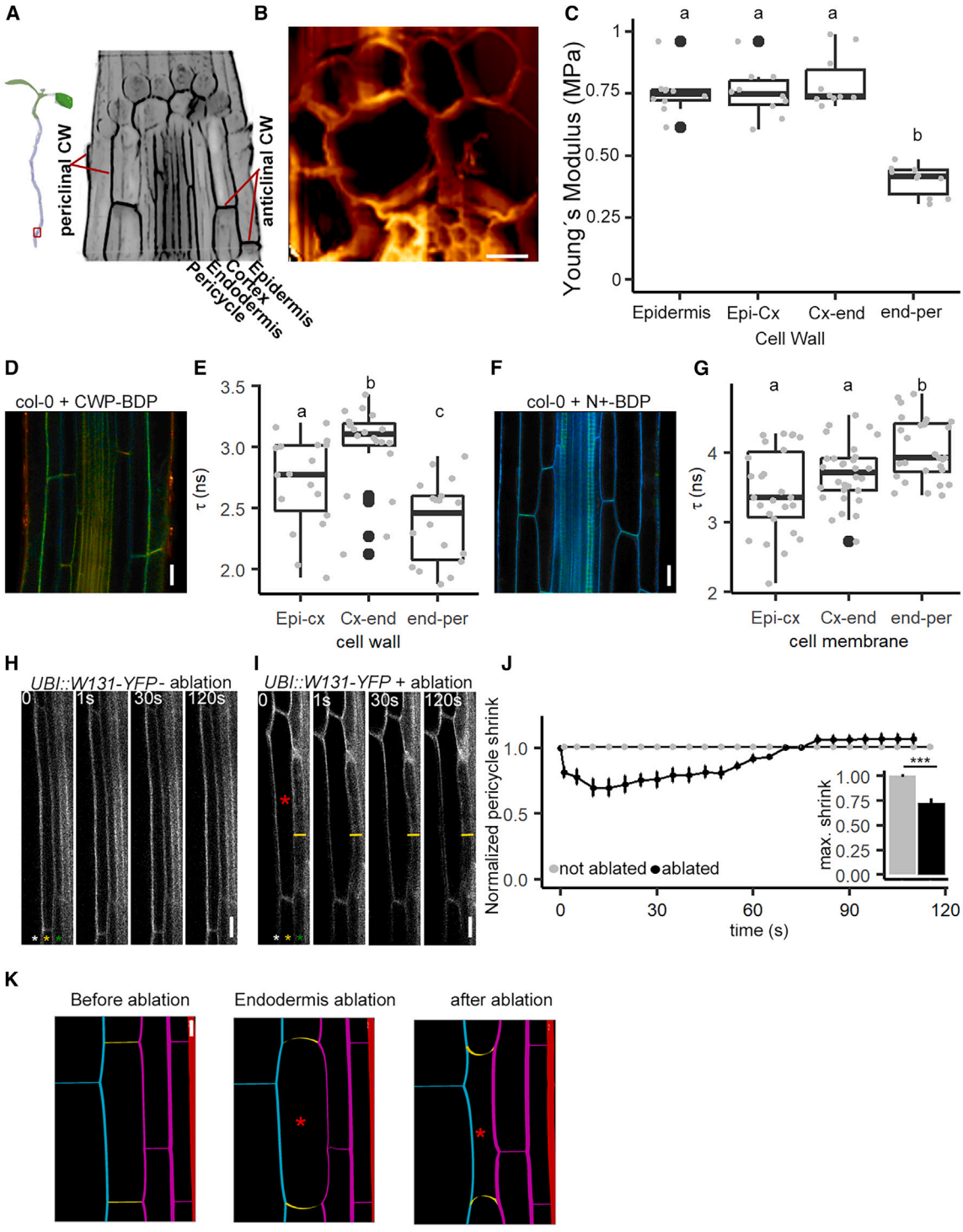


**Figure 1. In primary root, different mechanical properties are observed in the CW for each cell layer**

(A) Illustration of *Arabidopsis* primary root. Cell type longitudinal sections anticlinal and periclinal CW are shown.

(B) Topology AFM image displaying the cross-section of Col-0 roots. Scale bar, 5 μm.

(C) Quantification of the apparent Young's modulus in the CW of different cell layers in Col-0 roots. The center line and error bars represent the means ± SD obtained from at least three independent biological replicates for each cell layer type. Letters "a" and "b" indicate statistically significant differences based on one-way analysis of variance (ANOVA) and Tukey's honestly significant difference (HSD) test ($\alpha = 0.05$).

(D–G) Microviscosity maps of the CW (D and E) and plasma membrane (F and G) in the primary root. (D) Fluorescence lifetime microviscosity maps illustrating CWs (CWP-BDP) in *Arabidopsis* roots. Scale bar, 5 μm. (E) Quantification of the fluorescence lifetime microviscosity maps (D) expressed as photon lifetime in

*(legend continued on next page)*

once transduced across the CW into the cytoplasm, regulate downstream signaling pathways involved in the wound response.[8] Tissue restoration in the root apical meristem, the site at which daughter cells proliferate through transverse/anticlinal divisions (i.e., perpendicular to the root axis), is controlled by the hormone jasmonate.[12] However, as shown in previous research, severe damage to even a single cell can switch the orientation of cell division from transverse/anticlinal to periclinal (i.e., parallel to the root axis).[19] The periclinal divisions occur on the side adjacent to the wound, in a fashion that is similar to the regeneration of the entire root.[20,21] The high cellular regenerative potential observed in the root apical meristem can be explained by the possibility of activating cell division across all cell layers of the apical meristem.[10,11,19] However, this regenerative potential rapidly decreases away from the core stem cell niche.[19,20] In the differentiation zone of the root, only the xylem pole pericycle cells can divide in periclinal orientation after single-cell ablation in the adjacent endodermis.[20] During post-embryonic organogenesis, xylem pole pericycle cells produce lateral roots through a complex auxin-mediated process.[21,22]

The findings of the present study identify that—within the root—pericycle CWs are unique because they are under tension from vascular tissue, as well as subjected to compression from outer cell layers, which have lower CW elasticity at the tissue level. When an endodermal cell is damaged, this combination of forces results in pericycle cell deformation and subsequent cell division. Here, we find that the dynamic nature of the pericycle CW is highly dependent on pectin, whereas ethylene is required for proper cell division patterns. Given the crucial role of mechanical cues in cell division and tissue regeneration, our study provides evidence on how plants respond to damage at the cellular level. By focusing on the pericycle CWs in *Arabidopsis*, we expand existing knowledge about how physical forces influence cell division patterns and shed light into the fundamental processes of plant development and regeneration.

## RESULTS

### Inner and outer cell files demonstrate CW interface differences

Cell expansion is a critical developmental process that determines the final size and shape of plant organs.[23–25] In the xylem pole pericycle, cell expansion (swelling) occurs before the first asymmetric division (founder cells), leading to an increase in cell volume without a significant change in the volume of the overlying endodermal cells.[4] The sustained pressure from an expanded pericycle cell on the CWs of endodermal cells led us to hypothesize that root CWs may have specific properties.[7] To test this hypothesis, we used atomic force microscopy (AFM) to measure the elasticity, Young's modulus (E), of the CW in response to indentation (apparent stiffness). We determined the E of periclinal CWs (Figure 1A) in cross-sections of "live" *Arabidopsis* primary roots embedded in low melting agar (LMA) (~1 mm from the root apical meristem) (Figures 1B, 1C, and S1A). The AFM data showed that the CWs of outer cell files, such as those at the cortex-epidermis (epi-cx) and cortex-endodermis (cx-end) interfaces, were less elastic than inner cell files, such as the endodermis-pericycle (end-per) interface (Figure 1C). Interestingly, we did not observe significant differences between the epi-cx and cortex-endodermis interfaces (Figure 1C). As a control to test changes in CW elasticity, we measured with the cellulose biosynthesis inhibitor isoxaben (ISX), as outlined in Bacete et al.[26] The effects of ISX treatment of meristematic epidermal cells were subsequently examined using AFM (Figure S1B). Col-0 seedlings treated with ISX for 24 h exhibited reduced apparent stiffness compared with untreated Col-0 roots. Moreover, we confirmed a similar trend of CW elastic properties in fixed *Arabidopsis* and tomato embedded in LR white resin (Figures S1C–S1H). Interestingly, the CW elasticity is not necessarily correlated with the CW thickness (Figures S1I–S1K), while the outer epidermal wall is considerably thicker compared with the other CWs. To follow up on these results, we used mechanosensitive plasma membrane and CW probes[27] that detect changes in the mechanical environment based on shifts in fluorescence lifetime. The observed increase in the fluorescence lifetime of deeper tissue layers indicates increased membrane tension levels[28] (Figures 1D–1G). This observation, when considered together with the distinct changes in CW porosity measured by the CW mechanoprobe, highlights the particular properties of the pericycle cell layer from a mechanical perspective.

### Dynamics of pericycle CWs in response to laser ablation

Next, we investigated the role of differentiated elastic properties of CWs in the plant stress response based on single-cell-level experiments. To achieve this, we used a single-cell laser ablation technique followed by the high-resolution spatiotemporal analysis of subsequent cell shape changes (Figures 1H–1J). We did not observe any transitional changes in the width of the cortex following the ablation of an epidermal cell (Figure S2A; Video S1). In contrast, when a cortical cell was ablated, the adjacent endodermal cell expanded by an average of 15%, relative to the original width, in the direction of the ablated cell (Figure S2B; Video S1). Intriguingly, the laser ablation of a single endodermal cell caused the endodermal cell to instantaneously

nanoseconds. (F) Fluorescence lifetime microviscosity maps displaying cell membranes (N+-BDP) in *Arabidopsis* roots. Scale bar, 5 μm. (G) Quantification of the fluorescence lifetime microviscosity maps (F) expressed as photon lifetime in nanoseconds. The center line and error bars represent the means ± SD obtained from at least 20 different cells for each cell layer type. Letters "a"–"c" indicate statistically significant differences based on ANOVA and Tukey's HSD test ($\alpha$ = 0.05). BDP, BODIPY.

(H) Monitoring the width of pericycle cells without endodermal ablation in the plasma membrane marker UBI::W131-YFP line

(I) Monitoring the width of pericycle cells after ablation of the adjacent endodermal cell in the plasma membrane marker UBI::W131-YFP line. Scale bar, 5 μm.

(J) Quantification of the change in pericycle width after endodermal ablation. The inset shows the maximum shrinkage value measured 10 s after ablation. All values represent means ± SD. $n$ = 50 obtained from at least three independent biological replicates. Asterisks indicate statistically significant differences compared with the non-ablated cell (Student's t test, $^{**}p < 0.01$; $^{***}p < 0.001$; ns, not significant).

(K) Finite element model demonstrating longitudinal section of endodermal and pericycle deformation after endodermal ablation. The white asterisk corresponds to the cortical cell, the yellow asterisk corresponds to the endodermal cell, and the green asterisk corresponds to the pericycle cell. The red asterisk indicates the cell ablated. Abbreviations are as follows: epi, epidermis; cx, cortex; end, endodermis; and per, pericycle.

expand before collapsing. This dynamic expansion exerted transitional mechanical pressure on the adjacent pericycle cell: specifically, a bending of the endodermis-pericycle wall is observed. As a result, the diameter of the affected pericycle cell decreased by up to 40% compared with the unaffected, mock cell (Figures 1H–1J; Video S2). This reduction in pericycle width occurs in the first 10 s after endodermal ablation; after 2 min, the pericycle cell width returns to the initial state before endodermal ablation. It is interesting to note that the ablation of the endodermis generates an expansion that also causes pressure on the cortex-endodermis CW, however the reduction in the diameter of the cortical cell is only 10% (Figures S2C and S2D). These results reinforce the idea of an asymmetry of the CW elastic properties on the two faces of the endodermis. Following ablation, the endodermal cell expands into the neighboring cells before contracting. It could be presumed that this was the result of either heat released by the ablation laser before cell rupture or vibration of the CW. To further test how single-cell ablation affects cell expansion, we developed a 3D finite element method (FEM) model of the *Arabidopsis* root.[29,30] We initially raised turgor pressure by 2-fold and then released the pressure in the FEM model (Figure 1K; Video S3). As observed in the previous experiments, the endodermal cell in the model bulges more into the pericycle cells than into the cortical cells, even though pericycle cells are smaller. This further suggests that the CWs present at the endodermal-cortex interface are stiffer and under higher tension than those of cells at other cell files in the *Arabidopsis* primary root. Moreover, this finding provides further support to the observed differences in CW stiffness between various cell files in *Arabidopsis* roots and highlights the importance of the CW in determining the mechanical behaviour of root cells.

We also tested two scenarios when attempting to reproduce the observed behaviour following singe-cell ablation, namely (1) a model with uniform stiffness (Figure S2E) and (2) a model in which the outer epidermal and epidermis-cortex layers were 10 times stiffer than the other CWs (Figure S2E). This is a simplification of the model of Fridman et al.,[7] who have proposed that these walls have an enhanced role in regulating lateral growth in the root. In the uniform case, ablation of a cortical cell resulted in excessive bulging from the underlying endodermal cell, a phenomenon that is not observed in the differential stiffness model. When an endodermal cell was ablated, the model result was that the cortical cell above it also showed excessive bulging (Figure S2E); it is important to note that this was not observed in the previous *in silico* experiments (Figure 1K). When the model was applied to the ablation of a cortical cell, there was minimal bulging from the epidermal cell in both scenarios. This can be attributed to the fact that the epidermal cell, which is situated on the outer side of the cell layer, is subjected to stretching, whereas the cortical cell, which lies beneath, is ablated. However, it is important to highlight that—in the stiffer model—the ablation of an endodermal cell leads to an outward shift of the pericycle cells below, which was not observed in the uniform case. From these results, we concluded that the CWs of cells at the endodermis-cortex interface are likely stiffer than those of other pericycle cells.

Furthermore, we explored the impact of a slight reduction in cell volume on pericycle shrinkage (Figures S2F–S2H). For this reason, we introduced mild osmotic stress via treatment with 50 mM NaCl for 30 min, and we performed endodermal ablation upon observing the initial signs of plasmolysis (Figures S2F). Interestingly, no discernible differences were observed in the shrinkage response of the pericycle post ablation compared with mock plants. However, the recovery time for gaining original volume exhibited variations from the observed pattern in mock plants (Figure S2H), suggesting that the changes in cell volume are important during this subsequent phase of recovering the original diameter. We also evaluate whether cell geometry contributes to the shrink post endodermal ablation. We assessed pericycle shrinkage in Col-0 seedlings with varying cell lengths (Figures S2I and S2J). Short cells, not exceeding 60 μm in length, and long cells, reaching up to 170 μm in length, displayed a consistent shrinkage response following post-endodermal ablation. In parallel with ablation experiments involving cells of varying lengths (Figure S2K), the FEM model was applied to cells with different lengths as well (Figure S2L). Both the FEM model and the ablation experiments consistently demonstrated that the cell length does not influence the CW flexibility.

## The role of pectin in determining CW elasticity

Plant CW properties depend on a complex interplay of factors, including the composition of structural polysaccharides (cellulose, hemicelluloses, and pectin) and the degree of lignification and cross-linking between them.[31,32] Pectin plays a crucial role in cell adhesion, wall flexibility, and plant growth regulation, making it a pivotal component in shaping the structural and mechanical characteristics of plant CWs.[33,34] To investigate how the CW biochemical composition affects the mechanical properties, we analyzed the relative biochemical composition of the CW in each layer of the root using non-destructive confocal Raman microscopy.[35] Our results show that the pectin composition of endodermal cells differs from that of cortical and epidermal cells (Figures 2A and S3A; Table S1). This can be observed in the intensity of the peaks for the shift of 1,361 and 2,931 $cm^{-1}$, which correspond to the pectin C–H stretch. We also observed a difference in the shift of 1,440 $cm^{-1}$ assigned to acetyl esters $\delta_{as}(CH_3)$ in esterified pectin. This evidence implies that pectin may mediate the stretching of CW.[36,37] Unfortunately, reliable measurements of the composition of pericycle CWs could not be obtained due to methodological restrictions. In order to gain a comprehensive understanding of alterations in pectin localization and/or abundance, cross-sections were prepared from the mature zone of the root. These sections were subsequently labeled with specific antibodies: LM20, known for its recognition of high-degree methyl-esterified homogalacturonan (HG),[38] and LM19, an antibody that targets low-degree methyl-esterified HG.[38] The LM19 labeling exhibited uniform distribution across cross-sections. In contrast, LM20 labeling predominantly appeared in the vasculature CWs, indicating a distinct pectin distribution pattern in this area (see Figure S3B). This suggests variations in CW composition across different tissues, aligning with Wachsman et al.[39]

To identify the regulators of CW dynamics, we studied the pericycle cells of *Arabidopsis* roots harboring mutations in various CW biosynthesis and remodeling factors following the ablation of an endodermal cell (Figures 2B and 2C). Loss-of-function mutations in glycosyltransferases, which participate in the

CellPress
OPEN ACCESS

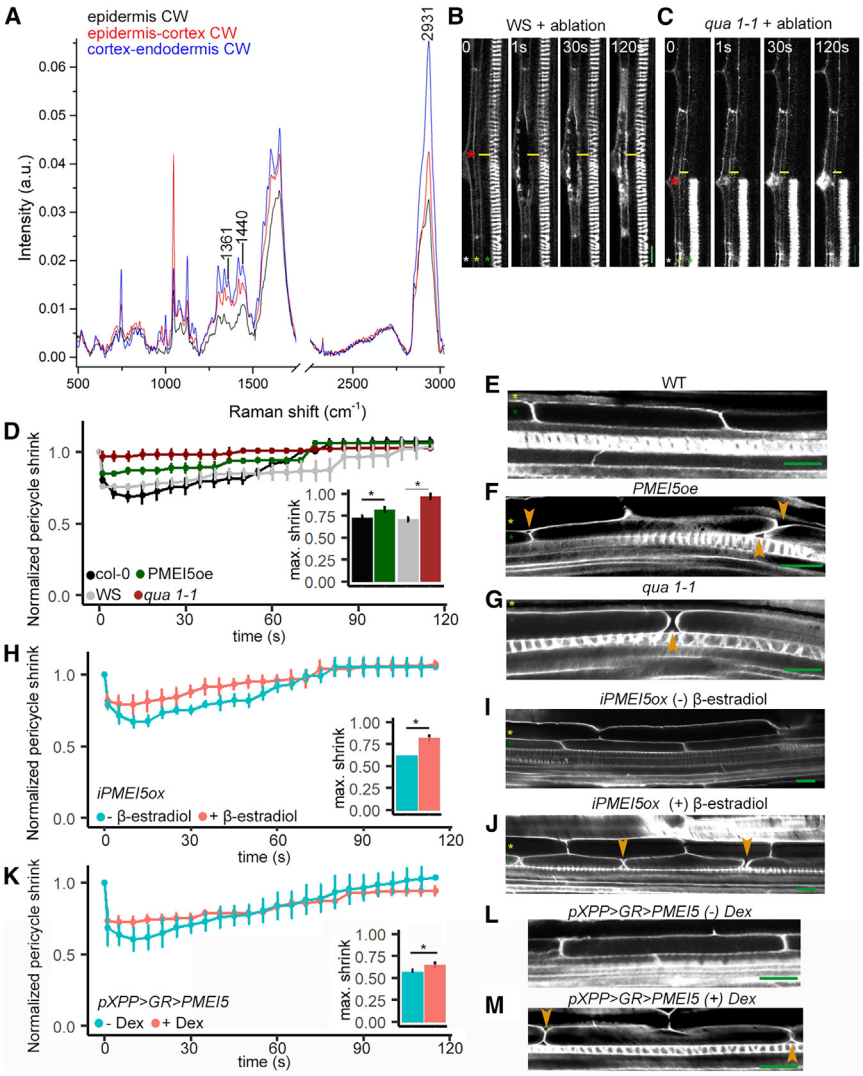


**Figure 2. Pectin mutants show impairment in pericycle shrinkage**

(A) Raman analysis of the CW (CW) in different cell layers. Raman spectra highlight the pectin peak at 1,361, 1,440, and 2,931 $cm^{-1}$. Semiquantitative analysis show variations in pectin levels among the different CWs.

(B) Monitoring the width of pericycle cells after ablation of the adjacent endodermal cell in WS roots stained with propidium iodide (PI). Scale bar, 5 μm.

(C) Monitoring the width of pericycle cells after ablation of the adjacent endodermal cell in *qua 1-1* roots stained with PI.

(D) Quantification of the change in pericycle width after endodermal ablation in Col-0, WS, *qua 1-1*, and PMEI5oe roots. The inset shows the maximum shrinkage value measured 10 s after ablation. All values represent means ±SD. $n$ = 30 obtained from at least three independent biological replicates. Asterisks indicate statistically significant differences compared with the non-ablated cell (Student's t test, $^{*}p < 0.05$; $^{**}p < 0.01$; ns, not significant).

(E–G) Pectin mutants exhibit varying levels of impaired cell-cell adhesion. The orange head arrow indicates sites of impaired cell adhesion. Roots were fixed and stained with calcofluor white. The red asterisk indicates the ablated cell. The white asterisk corresponds to the cortical cell, the yellow asterisk corresponds to the endodermal cell, and the green asterisk corresponds to the pericycle cell. Scale bars: 5 μm.

(H) Quantification of the change in pericycle width after endodermal ablation in inducible PMEI5ox line. The inset shows the maximum shrinkage value measured 10 s after ablation. All values represent means ±SD. $n$ = 30 obtained from at least three independent biological replicates. Asterisks indicate statistically significant differences compared with the non-ablated cell (Student's t test, $^{*}p < 0.05$; $^{**}p < 0.01$; ns, not significant).

(I and J) Inducible PMEI5ox (iPMEI5ox) treated with β-estradiol exhibit varying levels of impaired cell-cell adhesion. Scale bar, 5 μm.

(K) Quantification of the change in pericycle width after endodermal ablation in pXPP>GR>PMEI5 line treated or not with 50 μM Dex. The inset shows the maximum shrinkage value measured 10 s after ablation. All values represent means ±SD. $n$ = 30 obtained from at least three independent biological replicates. Asterisks indicate statistically significant differences compared with the non-ablated cell (Student's t test, $^{*}p < 0.05$; $^{**}p < 0.01$; ns, not significant).

(L and M) Inducible pXPP>GR>PMEI5 treated with 50 μM Dex exhibit impaired cell-cell adhesion; scale bar, 5 μm. The orange head arrow indicates sites of impaired cell adhesion. Roots were fixed and stained with cell wall (CW).

biosynthesis of polysaccharides and glycoproteins such as QUASIMODO 1 (QUA1), can affect the biochemical properties of the CW, as impaired HG biosynthesis causes cell adhesion defects.[40,41] Interestingly, we observed that the mutant *qua1-1*[40] showed a complete loss of transitional dynamics in the pericycle CW following the ablation of an endodermal cell (Figures 2B–2D). Similarly, cells with overexpression of pectin methyl esterase inhibitor 5 (PMEI5oe) expressed in all tissues, which limits de-methylesterified pectin,[42] demonstrated impaired cell-cell adhesion that ultimately inhibited CW dynamics (Figures 2E–2G). To further confirm a causal link between the pericycle diameter shrinkage phenotype and alterations in pectin levels, and to mitigate the potential influence of pleiotropic and compensatory effects, we employed the iPMEI5ox[42] estradiol-inducible lines. Before endodermal ablation, seedlings were treated with $\beta$-estradiol 12 h in advance and the subsequent pericycle diameter shrinkage was quantified (Figures 2H–2J). To further strengthen our findings, we used the tissue-specific, xylem pole pericycle line pXPP>GR>PMEI5.[43] We previously verified that dexamethasone (Dex) has no effect on the shrink response in Col-0 plants incubated for 24 h with Dex 50 μM (Figure S3C). Prior to endodermal ablation, seedlings were treated with Dex in advance and the subsequent pericycle diameter shrinkage was quantified (Figure 2K). Pericycle cells with induced PMEI5 expression demonstrated impaired cell-cell adhesion that ultimately reduced CW dynamics (Figures 2K–2M). Overall, our results showed a notable reduction in the shrinkage phenotype in $\beta$-estradiol- and Dex-treated seedlings compared with the mock roots, providing

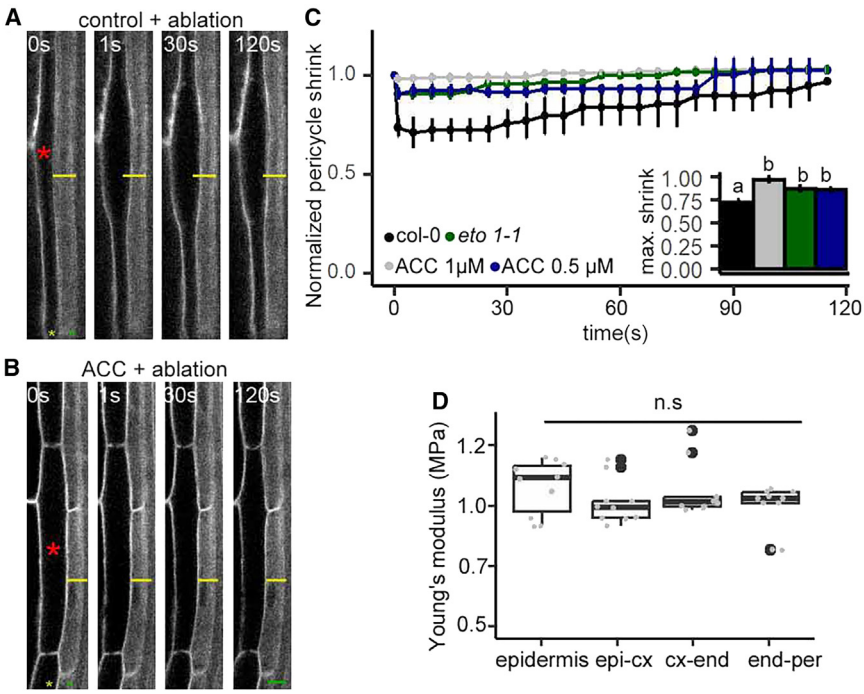


**Figure 3. Ethylene inhibits pericycle shrink by the regulation of CW biomechanics**

(A) Monitoring the width of pericycle cells after ablation of the adjacent endodermal cell in the plasma membrane marker UBI::W131-YFP line.

(B) Pericycle shrinkage after endodermal ablation in 5-day-old seedling treated width 1 μM of ACC for 18 h. Scale bar, 5 μm.

(C) Quantification of the change in pericycle width after ablation of the endodermis. Dose-response effect of ethylene on pericycle cell shrink. The inset shows the maximum shrinkage value measured 10 s after ablation. All values represent means ±SD. $n$ = 30 obtained from at least three independent biological replicates. Letters a and b indicate statistically significant differences according to ANOVA and Tukey's HSD test ($\alpha$ = 0.05).

(D) Quantification of the apparent Young's modulus in the CW of different cell layers. Center line and error bars indicate means ± SD from at least 3 independent biological replicates for each type of cell layer. No statistically significant differences were found between different cell layers according to ANOVA and Tukey's HSD test ($\alpha$ = 0.05).

support to the hypothesis that pectin plays a pivotal role in this process.

We also tested other well-described CW mutants (Figures S3D–S3F) and observed partial loss of CW dynamics in the PROCUSTE 1 mutant (*prc1-1*), as under basal conditions. The *PROCUSTE 1* gene encodes CELLULOSE SYNTHASE 6 (Figure S3D), which is critical for cellulose synthesis in the primary CW.[44] Next, we investigated mutants characterized by a deficiency in the *de novo* synthesis of single monosaccharides.[45] The arabinose-deficient *mur 4-1* mutant[46] demonstrated reduced pericycle CW dynamics, whereas the *mur 9-1* (fucose- and xylose-deficient), *mur 1-2* (completely lacking fucose), and *mur 11-1* (rhamnose-, fucose-, and xylose-deficient) mutants did not show significant differences in CW dynamics when compared with Col-0 cells[47] (Figure S3E). Furthermore, we investigated CW receptors responsible for CW integrity and sensing of mechanical stimuli. We found a partial loss of mechanical elasticity in the triple mutant defective in LEUCIN RICH REPEAT/EXTENSIN3/4/5, THESEUS1, and FEI1/2 (*lrx 3-4-5/the 1-1/fei1-2*) (Figure S3F). However, the FERONIA mutant *fer-4*[14,48–50] did not show any significant differences in mechanical elasticity when compared with the Col-0. This suggests that certain mechano-sensors partially contribute to CW dynamics following an injury of the root. FEI1/2 transmits a pectin breakdown signal, leading to the production of 1-aminocyclopropane-1-carboxylic acid (ACC), a precursor of ethylene, which has profound effects on physiological responses in plants.[40–51] Furthermore, ACC/ethylene have been implicated in CW integrity maintenance.[52] This led us to investigate the role of ACC/ethylene in regulation of CW dynamics (Figure S4). Using Raman microscopy, we were able to observe changes in the composition of the CW in seeds treated with ACC (Figures S3G–S3J; Table S1). Later, we tested whether seedlings treated with the ethylene precursor ACC show impaired CW dynamics after the ablation of endodermal cells (Figures 3A–3C and S3K–S3M). Our results show that ACC treatment severely reduced CW dynamics in a concentration-dependent manner when compared with non-treated seedlings or seedlings that had been treated with other phytohormones (Figures S3K and S3L). We confirmed changes in CW E by AFM measurements (Figures 3D, S4A, and S4B), where all of the CWs had a similar E; the elastic properties were also found to be correlated with the pectin levels, observed for the 1,440 $cm^{-1}$ shift and the 2,931 $cm^{-1}$ shift, and in the treatment with ACC the quantitative relative values are similar for each type of cell (Figures S3G–S3J and S4B; Table S1). In addition, we tested mutants characterized by a defective ethylene metabolism, e.g., the ETHYLENE OVERPRODUCER 1 mutant *eto 1-1*[53] and the ETHYLENE INSENSITIVE (EIN) signaling pathway mutants *ein 2-1*, *ethylene response-1* (*etr-1-1*), and *ein 3-1*,[54] for changes in their CW dynamics after ablation (Figures 3B and S3M). Among these mutants, only *eto 1-1,* which has a high level of endogenous ethylene,[53] showed a loss of CW dynamics among pericycle cells after damage to the endodermis (Figure 3C). These results suggest that ethylene modifies the biochemical properties of the CW; more specifically, this phytohormone can affect the biomechanical composition properties of the CW and potentially alter the cell-cell transmission of positional cues.

## Ethylene-controlled CW dynamics are required for patterned cell division

Dynamic changes in xylem pole pericycle cells have been observed prior to the first formative division of the lateral root primordium.[4,20] To investigate whether the CW mechanical properties influence the orientation of cell division, we performed targeted ablations in endodermal cells. We used a microtubule reporter line to obtain *in vivo* observations of cell division orientation; the reporter line expresses a microtubule-binding domain

CellPress
OPEN ACCESS

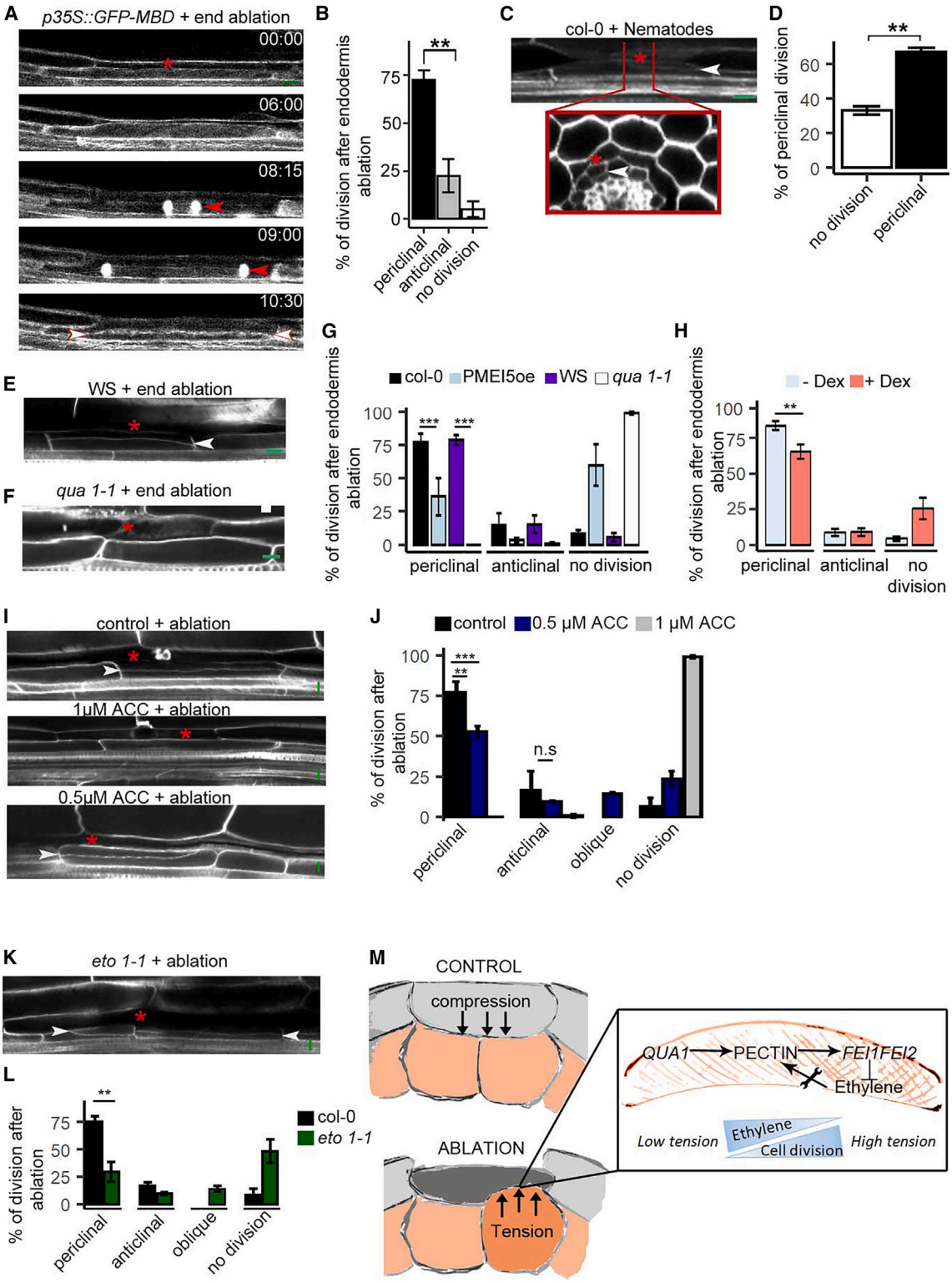


**Figure 4. Division of pericycle cell after local damage**

Pericycle division was observed following ablation of the adjacent endodermal cell (A) or pericycle cell. The direction of cell plate expansion was visualized using the microtubule 35S::MBD-GFP reporter (indicated by red arrowheads, whereas white arrowhead with red outline indicates new cell plate) Scale bar, 5 μm. (A) Periclinal division of the pericycle was observed after endodermal ablation.

*(legend continued on next page)*

(MBD) fused to GFP and driven by the 35S promoter from the cauliflower mosaic virus.[55] Following endodermal cell ablation, 73% of the division events led to periclinal divisions in the adjacent pericycle cells, whereas only 23% of the division events resulted in transverse/anticlinal cell division (Figures 4A and 4B). To confirm these results, we infected plants with cyst nematodes, which migrate intracellularly and leave a trail of mechanically damaged cells.[56] 48 h after nematode infection, we observed the orientation of cell divisions (Figures 4C and 4D). We focused on root areas with minimal damage, i.e., only a few cells had been injured, and observed predominantly periclinal divisions (Figures 4C and 4D), a finding that mirrored the outcomes of single-cell endodermal ablation (Figures 4A and 4B). This result confirms that the use of laser ablation, which artificially induces cellular damage, has biological relevance for studying naturally occurring tissue damage during various events, e.g., pathogen attack. We performed experiments with *qua1-1* and PMEI5oe mutants to further confirm that the observed periclinal cell divisions are a result of shifting CW mechanical dynamics. Remarkably, no divisions of pericycle cells were observed in *qua 1-1* mutants, even 24 h after endodermal ablation, whereas the PMEI5oe mutants showed a lower degree of regeneration when compared with Col-0 plants (Figures 4E–4G). Similar results were observed in the regeneration rate of the pXPP>GR>PMEI5 line under Dex treatment (Figure 4H). In the same sense, we observed a lower degree of regeneration in more mutants related to the CW, showing that different compounds of the CW participate in the wound sensing (Figures S4C and S4D). This further supports the notion that mechanical stimulation plays a crucial role in initiating cell regeneration. Although a diverse chemical signaling cascade governs cell division in plants, the application of potassium iodide (KI) as a scavenger of $H_2O_2$ and EDTA in ablated cells did not exhibit any variations compared with the mock conditions (Figure S4E).

Ethylene is involved in cell division in the *Arabidopsis* root through ETR1, which activates the downstream transcription factors EIN3 and ETHYLENE-INSENSITIVE3-LIKE 1 (EIL1).[57] Furthermore, ethylene signaling has been suggested to regulate CW integrity maintenance.[58,59] We used two different concentrations of ACC (0.5 and 1 μM) to study patterns of cell division during regeneration. Interestingly, treatment with 1 μM of ACC led to the complete loss of pericycle CW dynamics and no cell divisions occurred prior to the ablation of an endodermal cell (Figures 4I and 4J) relative to seedlings treated with the ethylene inhibitor aminoethoxyvinylglycine (AVG) and untreated mock seedlings (Figures S4F and S4G). However, roots treated with the lower concentration of ACC (0.5 μM) regained the regenerative capacity of pericycle cells, resulting in predominantly periclinal divisions, with 15% of the cell divisions having an oblique orientation (Figures 4I and 4J). As was the case with ACC-treated seedlings, *eto1-1* mutants showed a low rate (15%) of oblique cell divisions after endodermal cell ablation (Figures 4K and 4M). These results support our findings that correlate with the orientation of cell divisions during regeneration. In addition, we provide evidence that the pattern of cell division orientation is finely regulated by ethylene.

## DISCUSSION

Physical damage is an inherent aspect of the life cycle of a plant, yet our understanding of the mechanisms underlying the remarkable regenerative ability of plants remains incomplete. Here, we focused on investigating the coordination between CW flexibility and cell division at the cellular level in response to single-cell wounds. The observed asymmetry in CW elastic properties between the two faces of the endodermis plays a significant role in transitional wall bending, which sets the stage for subsequent cellular activities. This bending influences the mechanical environment, facilitating specific division patterns later in the regeneration process. More specifically, our data demonstrate that pericycle cells, which are characterized by more elastic CWs, play a pivotal role in regulating cell expansion, division rates, and the transduction of wound signals (Figure 1). The activation of the *qua 1-1*, PMEI5oe, iPMEI5ox, and pXPP>GR>PMEI5 lines defective in pectin and exhibiting impaired cell-cell adhesion supports the notion that mechanical

(B) Quantification of the number of divisions occurring within 16 h after endodermal cell ablation, means ± SD. $n = 50$ obtained from at least three independent biological replicates (Wilcoxon paired test, $^{**}p < 0.01$; $^{***}p < 0.001$; ns, not significant).
(C) Representative image of pericycle cell division after seedlings were infected with cyst nematodes for 48 h. Roots were fixed and stained with calcofluor white. Scale bar, 5 μm.
(D) Quantification of the number of divisions after nematode damage, means ± SD. $n = 20$ obtained from at least three independent biological replicates (Wilcoxon paired test, $^{**}p < 0.01$; $^{***}p < 0.001$; ns, not significant).
(E and F) Periclinal division in pericycle cells after endodermal ablation in WS and *qua 1-1* seedlings. Roots were fixed and stained with calcofluor white. Scale bar, 5 μm.
(G) Quantification of periclinal division in Col-0, PMEI5oe, WS, and *qua1-1*, means ± SD. $n = 30$ obtained from at least three independent biological replicates. All values represent means ± SD. Asterisks indicate statistically significant differences (Wilcoxon paired test, $^{**}p < 0.01$; $^{***}p < 0.001$; ns, not significant).
(H) Quantification of periclinal division in pXPP>GR>PMEI5 treated or not with 50 μM Dex means ± SD, $n = 30$. Quantification of the number of divisions occurring within 10 h after endodermal cell ablation. Asterisks indicate statistically significant differences (Wilcoxon paired test, $^{**}p < 0.01$; $^{***}p < 0.001$; ns, not significant).
(I) Pattern division in pericycle cell after endodermal ablation in seedling treated with 0.5 or 1 μM ACC. Oblique divisions were found in low concentrations of ACC. Scale bar, 5 μm.
(J) Quantification of (I) means ± SD. $n = 30$ obtained from at least three independent biological replicates. Asterisks indicate statistically significant (Wilcoxon paired test, $^{**}p < 0.01$; $^{***}p < 0.001$; ns, not significant).
(K) Ablation in endodermis or pericycle cell in *eto1-1* show oblique division. Scale bar, 5 μm.
(L) Quantification of (K). Means ± SD. $n = 30$ obtained from at least three independent biological replicates (Wilcoxon paired test, $^{**}p < 0.01$; $^{***}p < 0.001$; ns, not significant).
(M) A schematic model of mechano-chemical feedback during regeneration. The endodermal cell layer is shown in gray. In dark gray, the ablated endodermal cell is observed. In orange, the pericycle cells are observed, and in dark orange, the swollen pericycle cell. The inset shows the CW of the pericycle cell after expansion. Red asterisk: cell ablated; white arrowheads: new CW.

inputs from neighboring cells are necessary for sensing pressure changes and initiating cell division during regeneration (Figures 2 and 4). Furthermore, our results show that an increase in ethylene levels, either by genetic means or exogenous ACC treatment, restricts CW flexibility and leads to impaired regeneration (Figure 3). The involvement of the FEI 1,2 receptors, which regulate ethylene levels in response to mechanical stimuli and participate in maintaining pectin integrity,[49] further supports the idea that ACC/ethylene play a crucial role in promoting regeneration upon wounding. Additionally, the *qua 2-1* mutant, which was characterized by reduced galacturonic acid levels, exhibited decreased *FEI 1* and *2* expression,[60] a result that outlines the existence of a feedback loop between pectin composition, CW integrity, and ethylene signaling (Figure 4L). Overall, our data highlight how plant roots transmit information via mechanical forces in an extracellular matrix, including CWs of varying rigidities, which enables cells to bulge into wounded regions and determine the cell division plane to ultimately shape the architecture of repaired tissue.

### Limitations of the study

The limitations of the present work are as follows. Single-cell laser ablation is a powerful tool to study the role of mechanical cues in cellular physiology in deep tissue such as pericycle cells. However, the fast response in changing cell shape gives rise to different interpretations, and more in-depth analysis is necessary to improve the understanding of this phenomenon. Plant cells exert turgor pressure: when we ablate an endodermal cell, the turgor pressure is redistributed to the surrounding CWs. By considering the size of the cells and applying the principle of parsimony, we can infer that the pressure after endodermal ablation is equal on both the cortex wall and the pericycle wall. Therefore, the variation in the degree of bending in these walls is attributable to the mechanical properties of the CWs themselves. An alternative explanation is that the endodermal cell is under radial tension from the cortical and pericycle cells, and when ablated, the adjacent cortical and periclinal cells "pull" the endodermal gap open instead of it "pushing" into the neighboring cells.

Although our study provides sufficient resolution, allowing for deeper insights into the chemical and mechanical properties of adjacent CWs through techniques like Raman spectroscopy and AFM, there are needs for refinement in this aspect.

The biochemical and compositional study of the CW presents a significant challenge. Although good spatial resolution results of CW composition in different models have been presented for over a decade, these models predominantly involve secondary CWs in various organisms. Secondary CWs are significantly thicker than the primary CWs of *Arabidopsis* root cells. Although we do not dismiss the possibility that differences in CW thickness might affect Raman measurements, we used a 50× NA (numerical aperture) = 0.5 objective, where the resolution is in the order of micrometers (μm), and the differences in CW thickness are in the order of nanometers (nm). Therefore, we consider these differences to be below the sensitivity threshold of Raman spectroscopy. Nonetheless, this point should be considered for future studies, which will involve optimizing measurements in smaller samples, such as *Arabidopsis* root cells.

A similar analysis can be conducted using the immunohistochemistry technique. When cross-sections are incubated with antibodies (Ig), they are abundant and have access to the CW regardless of the position within the root. The results presented in this study align with previous findings from other laboratories, such as Wachsman et al.[39] (in root) and Kuczak 2020[61] (hypocotyl).

Second, the molecular signaling mechanisms underlying the observed phenomena have yet to be fully identified. This represents a significant avenue for future research to elucidate the intricate pathways and interactions governing these processes. Moreover, a crucial question for future inquiry revolves around understanding how the single CW responses connect to organismal function. By exploring this connection, we can gain a more comprehensive understanding of the biological significance and implications of our findings.

## RESOURCE AVAILABILITY

### Lead contact

Further information and requests for resources and reagents should be directed to and will be fulfilled by the lead contact, Peter Marhavy (peter.marhavy@slu.se).

### Materials availability

Further information and requests for resources and reagents listed in key resources table should be addressed to the lead contact.

### Data and code availability

All the microscopy data generated and analyzed for this study have been deposited at the Swedish National Data service https://doi.org/10.5878/c1gs-8272.

This paper does not report original code. Any additional information required to reanalyze the data reported in this paper is available from the lead contact upon request.

## ACKNOWLEDGMENTS

We would like to thank Niko Geldner, Eva Benkova, Rishikesh Bhalerao, and Vaughan Hurry for their valuable comments on the manuscript. Furthermore, we thank Stephanie Roberts, Stephane Verger, Rishikesh Bhalerao, and Sebastian Wolf for sharing published materials. We would also like to thank George Kenanakis from the Photonic, Phononic- and Meta-Materials Laboratory of the Institute of Electronic Structure and Laser at FORTH for granting access to the Raman spectroscopy instrument. We acknowledge the Plant Growth and Microscopy facilities at UPSC for their assistance with the research. This work was supported by funds that had been allocated to P.M. (Vetenskapsrådet grant 2019-05634, Carl Tryggers CTS 20:277, Kempestiftelserna JCK-2011 and JCSMK22-0091, Knut and Alice Wallenberg Foundation [KAW 2022.0029-Fate]); M.S.C.A. (Marie Currie Individual Postdoctoral fellowship [PREENER-101066035]); P.N.M. (EU Marie Curie-RISE ["PANTHEON," 872969]); A.M. (Hellenic Foundation of Research and Innovation PhD scholarship [06526], BBSRC Institute Strategic Programme grant to the John Innes Centre [BB/X01102X/1]); R.S.S. (German Research Council grant [ERA-CAPS V-MORPH]); and N.T. (John Innes Foundation funding). J.S. and M.B. are supported by an European Research Council (ERC CoG grant, grant number: 101000981).

## AUTHOR CONTRIBUTIONS

P.M. initiated the project, while L.M.D.F. planned, designed, and conceived the project with input from P.M. L.M.D.F. and P.M. wrote the manuscript with input from the other authors. L.M.D.F. performed the single-cell ablation assay, along with the AFM measurements and data analysis. M.S.A. performed root infection with nematodes. X.M. conducted the mutant root phenotyping. N.Z. performed data analysis. M.B. and J.S. performed the FLIM

imaging and analyses with mechanoprobes. A.M., V.P., and P.N.M. conducted the inmunostaining and Raman measurements and the corresponding analyses. L.A.B. and T.H. performed CW investigation. N.T., M.M., and R.S.S. performed the 3D computational modeling.

## DECLARATION OF INTERESTS

The authors declare no competing interests.

## STAR★METHODS

Detailed methods are provided in the online version of this paper and include the following:

- KEY RESOURCES TABLE
- EXPERIMENTAL MODEL AND STUDY PARTICIPANT DETAILS
  - Plant materials
  - Plant growth condition
- METHOD DETAILS
  - Hormonal and drug treatment
  - Confocal imaging and real-time analysis
  - FLIM imaging and analysis
  - Histochemical staining
  - Single-cell laser ablation
  - Nematode infection
  - Atomic Force Microscopy
  - Transmission Electron Microscopy imaging
  - Resin Embedding and Sectioning
  - Tissue embedding and sectioning for immuno localization
  - Immunocytochemistry
  - Raman Microscopy
  - Mechano-probe synthesis
  - Model and Finite Element Model
- QUANTIFICATION AND STATISTICAL ANALYSIS

## SUPPLEMENTAL INFORMATION

Supplemental information can be found online at https://doi.org/10.1016/j.devcel.2024.12.032.

Received: August 15, 2023
Revised: March 15, 2024
Accepted: December 17, 2024
Published: January 13, 2025

## REFERENCES

1. Scheres, B., McKhann, H.I., and Van Den Berg, C. (1996). Roots Redefined: Anatomical and Genetic Analysis of Root Development. Plant Physiol. *111*, 959–964. https://doi.org/10.1104/pp.111.4.959.
2. Trinh, D.C., Alonso-Serra, J., Asaoka, M., Colin, L., Cortes, M., Malivert, A., Takatani, S., Zhao, F., Traas, J., Trehin, C., et al. (2021). How Mechanical Forces Shape Plant Organs. Curr. Biol. *31*, R143–R159. https://doi.org/10.1016/j.cub.2020.12.001.
3. Van Norman, J.M., Breakfield, N.W., and Benfey, P.N. (2011). Intercellular communication during plant development. Plant Cell *23*, 855–864. https://doi.org/10.1105/tpc.111.082982.
4. Vermeer, J.E.M., von Wangenheim, D., Barberon, M., Lee, Y., Stelzer, E.H.K., Maizel, A., and Geldner, N. (2014). A spatial accommodation by neighboring cells is required for organ initiation in Arabidopsis. Science *343*, 178–183. https://doi.org/10.1126/science.1245871.
5. Heisler, M.G., Hamant, O., Krupinski, P., Uyttewaal, M., Ohno, C., Jönsson, H., Traas, J., and Meyerowitz, E.M. (2010). Alignment between PIN1 polarity and microtubule orientation in the shoot apical meristem reveals a tight coupling between morphogenesis and auxin transport. PLoS Biol. *8*, e1000516. https://doi.org/10.1371/journal.pbio.1000516.
6. Bukoreshtliev, N.V., Haase, K., and Pelling, A.E. (2013). Mechanical cues in cellular signalling and communication. Cell Tissue Res. *352*, 77–94. https://doi.org/10.1007/s00441-012-1531-4.
7. Fridman, Y., Strauss, S., Horev, G., Ackerman-Lavert, M., Reiner-Benaim, A., Lane, B., Smith, R.S., and Savaldi-Goldstein, S. (2021). The root meristem is shaped by brassinosteroid control of cell geometry. Nat. Plants *7*, 1475–1484. https://doi.org/10.1038/s41477-021-01014-9.
8. Engelsdorf, T., Gigli-Bisceglia, N., Veerabagu, M., McKenna, J.F., Vaahtera, L., Augstein, F., Van der Does, D., Zipfel, C., and Hamann, T. (2018). The plant cell wall integrity maintenance and immune signaling systems cooperate to control stress responses in *Arabidopsis thaliana*. Sci. Signal. *11*, eaao3070. https://doi.org/10.1126/scisignal.aao3070.
9. Bacete, L., and Hamann, T. (2020). The Role of Mechanoperception in Plant cell wall Integrity Maintenance. Plants (Basel) *9*, 574. https://doi.org/10.3390/plants9050574.
10. Efroni, I., Mello, A., Nawy, T., Ip, P.L., Rahni, R., DelRose, N., Powers, A., Satija, R., and Birnbaum, K.D. (2016). Root Regeneration Triggers an Embryo-like Sequence Guided by Hormonal Interactions. Cell *165*, 1721–1733. https://doi.org/10.1016/j.cell.2016.04.046.
11. Ikeuchi, M., Favero, D.S., Sakamoto, Y., Iwase, A., Coleman, D., Rymen, B., and Sugimoto, K. (2019). Molecular Mechanisms of Plant Regeneration. Annu. Rev. Plant Biol. *70*, 377–406. https://doi.org/10.1146/annurev-arplant-050718-100434.
12. Zhou, W., Lozano-Torres, J.L., Blilou, I., Zhang, X., Zhai, Q., Smant, G., Li, C., and Scheres, B. (2019). A Jasmonate Signaling Network Activates Root Stem Cells and Promotes Regeneration. Cell *177*, 942–956.e14. https://doi.org/10.1016/j.cell.2019.03.006.
13. Miedes, E., Vanholme, R., Boerjan, W., and Molina, A. (2014). The role of the secondary cell wall in plant resistance to pathogens. Front. Plant Sci. *5*, 358. https://doi.org/10.3389/fpls.2014.00358.
14. Hématy, K., Sado, P.E., Van Tuinen, A., Rochange, S., Desnos, T., Balzergue, S., Pelletier, S., Renou, J.P., and Höfte, H. (2007). A receptor-like kinase mediates the response of Arabidopsis cells to the inhibition of cellulose synthesis. Curr. Biol. *17*, 922–931. https://doi.org/10.1016/j.cub.2007.05.018.
15. Scheller, H.V., and Ulvskov, P. (2010). Hemicelluloses. Annu. Rev. Plant Biol. *61*, 263–289. https://doi.org/10.1146/annurev-arplant-042809-112315.
16. Palin, R., and Geitmann, A. (2012). The role of pectin in plant morphogenesis. Biosystems. *109*, 397–402. https://doi.org/10.1016/j.biosystems.2012.04.006.
17. Cosgrove, D.J. (2018). Diffuse Growth of Plant cell walls. Plant Physiol. *176*, 16–27. https://doi.org/10.1104/pp.17.01541.
18. Hush, J.M., Hawes, C.R., and Overall, R.L. (1990). Interphase microtubule re-orientation predicts a new cell polarity in wounded pea roots. J. Cell Sci. *96*, 47–61. https://doi.org/10.1242/jcs.96.1.47.
19. Marhava, P., Hoermayer, L., Yoshida, S., Marhavý, P., Benková, E., and Friml, J. (2019). Re-activation of Stem Cell Pathways for Pattern Restoration in Plant Wound Healing. Cell *177*, 957–969.e13. https://doi.org/10.1016/j.cell.2019.04.015.
20. Marhavý, P., Montesinos, J.C., Abuzeineh, A., Van Damme, D., Vermeer, J.E.M., Duclercq, J., Rakusová, H., Nováková, P., Friml, J., Geldner, N., et al. (2016). Targeted cell elimination reveals an auxin-guided biphasic mode of lateral root initiation. Genes Dev. *30*, 471–483. https://doi.org/10.1101/gad.276964.115.
21. Moreno-Risueno, M.A., Van Norman, J.M., Moreno, A., Zhang, J., Ahnert, S.E., and Benfey, P.N. (2010). Oscillating gene expression determines competence for periodic Arabidopsis root branching. Science *329*, 1306–1311. https://doi.org/10.1126/science.1191937.
22. De Smet, I., Tetsumura, T., De Rybel, B., Frei dit Frey, N., Laplaze, L., Casimiro, I., Swarup, R., Naudts, M., Vanneste, S., Audenaert, D., et al. (2007). Auxin-dependent regulation of lateral root positioning in the basal meristem of Arabidopsis. Development *134*, 681–690. https://doi.org/10.1242/dev.02753.

23. Cosgrove, D.J. (2005). Growth of the plant cell wall. Nat. Rev. Mol. Cell Biol. *6*, 850–861. https://doi.org/10.1038/nrm1746.

24. Kutschera, U., and Niklas, K.J. (2007). The epidermal-growth-control theory of stem elongation: an old and a new perspective. J. Plant Physiol. *164*, 1395–1409. https://doi.org/10.1016/j.jplph.2007.08.002.

25. Perilli, S., and Sabatini, S. (2010). Analysis of root meristem size development. Methods Mol. Biol. *655*, 177–187. https://doi.org/10.1007/978-1-60761-765-5_12.

26. Bacete, L., Schulz, J., Engelsdorf, T., Bartosova, Z., Vaahtera, L., Yan, G., Gerhold, J.M., Tichá, T., Øvstebø, C., Gigli-Bisceglia, N., et al. (2022). THESEUS1 modulates cell wall stiffness and abscisic acid production in Arabidopsis thaliana. Proc. Natl. Acad. Sci. USA *119*, e2119258119. https://doi.org/10.1073/pnas.2119258119.

27. Michels, L., Gorelova, V., Harnvanichvech, Y., Borst, J.W., Albada, B., Weijers, D., and Sprakel, J. (2020). Complete microviscosity maps of living plant cells and tissues with a toolbox of targeting mechanoprobes. Proc. Natl. Acad. Sci. USA. *117*, 18110–18118. https://doi.org/10.1073/pnas.1921374117.

28. Ryder, L.S., Lopez, S.G., Michels, L., Eseola, A.B., Sprakel, J., Ma, W., and Talbot, N.J. (2023). A molecular mechanosensor for real-time visualization of appressorium membrane tension in Magnaporthe oryzae. Nat. Microbiol. *8*, 1508–1519. https://doi.org/10.1038/s41564-023-01430-x.

29. Bassel, G.W., Stamm, P., Mosca, G., Barbier de Reuille, P., Gibbs, D.J., Winter, R., Janka, A., Holdsworth, M.J., and Smith, R.S. (2014). Mechanical constraints imposed by 3D cellular geometry and arrangement modulate growth patterns in the Arabidopsis embryo. Proc. Natl. Acad. Sci. USA *111*, 8685–8690. https://doi.org/10.1073/pnas.1404616111.

30. Kelly-Bellow, R., Lee, K., Kennaway, R., Barclay, J.E., Whibley, A., Bushell, C., Spooner, J., Yu, M., Brett, P., Kular, B., et al. (2023). Brassinosteroid coordinates cell layer interactions in plants via cell wall and tissue mechanics. Science *380*, 1275–1281. https://doi.org/10.1126/science.adf0752.

31. Bashline, L., Lei, L., Li, S., and Gu, Y. (2014). Cell wall, cytoskeleton, and cell expansion in higher plants. Mol. Plant *7*, 586–600. https://doi.org/10.1093/mp/ssu018.

32. Wolf, S., Mouille, G., and Pelloux, J. (2009). Homogalacturonan methyl-esterification and plant development. Mol. Plant *2*, 851–860. https://doi.org/10.1093/mp/ssp066.

33. Caffall, K.H., and Mohnen, D. (2009). The structure, function, and biosynthesis of plant cell wall pectic polysaccharides. Carbohydr. Res. *344*, 1879–1900. https://doi.org/10.1016/j.carres.2009.05.021.

34. Harholt, J., Suttangkakul, A., and Vibe Scheller, H. (2010). Biosynthesis of pectin. Plant Physiol. *153*, 384–395. https://doi.org/10.1104/pp.110.156588.

35. Atalla, R.H., and Agarwal, U.P. (1986). Recording Raman spectra from plant cell walls. J. Raman Spectrosc. *17*, 229–231. https://doi.org/10.1002/jrs.1250170213.

36. Bosch, M., and Hepler, P.K. (2005). Pectin methylesterases and pectin dynamics in pollen tubes. Plant Cell *17*, 3219–3226. https://doi.org/10.1105/tpc.105.037473.

37. Gigli-Bisceglia, N., van Zelm, E., Huo, W., Lamers, J., and Testerink, C. (2022). Arabidopsis root responses to salinity depend on pectin modification and cell wall sensing. Development *149*, dev200363. https://doi.org/10.1242/dev.200363.

38. Verhertbruggen, Y., Marcus, S.E., Haeger, A., Ordaz-Ortiz, J.J., and Knox, J.P. (2009). An extended set of monoclonal antibodies to pectic homogalacturonan. Carbohydr. Res. *344*, 1858–1862. https://doi.org/10.1016/j.carres.2008.11.010.

39. Wachsman, G., Zhang, J., Moreno-Risueno, M.A., Anderson, C.T., and Benfey, P.N. (2020). Cell wall remodeling and vesicle trafficking mediate the root clock in *Arabidopsis*. Science *370*, 819–823. https://doi.org/10.1126/science.abb7250.

40. Bouton, S., Leboeuf, E., Mouille, G., Leydecker, M.T., Talbotec, J., Granier, F., Lahaye, M., Höfte, H., and Truong, H.N. (2002). QUASIMODO1 encodes a putative membrane-bound glycosyltransferase required for normal pectin synthesis and cell adhesion in Arabidopsis. Plant Cell *14*, 2577–2590. https://doi.org/10.1105/tpc.004259.

41. Verger, S., Chabout, S., Gineau, E., and Mouille, G. (2016). Cell adhesion in plants is under the control of putative O-fucosyltransferases. Development *143*, 2536–2540. https://doi.org/10.1242/dev.132308.

42. Wolf, S., Mravec, J., Greiner, S., Mouille, G., and Höfte, H. (2012). Plant cell wall homeostasis is mediated by brassinosteroid feedback signaling. Curr. Biol. *22*, 1732–1737. https://doi.org/10.1016/j.cub.2012.07.036.

43. Li, Z., Sela, A., Fridman, Y., Garstka, L., Höfte, H., Savaldi-Goldstein, S., and Wolf, S. (2021). Optimal BR signalling is required for adequate cell wall orientation in the Arabidopsis root meristem. Development *148*, dev199504. https://doi.org/10.1242/dev.199504.

44. Fagard, M., Desnos, T., Desprez, T., Goubet, F., Refregier, G., Mouille, G., McCann, M., Rayon, C., Vernhettes, S., and Höfte, H. (2000). PROCUSTE1 encodes a cellulose synthase required for normal cell elongation specifically in roots and dark-grown hypocotyls of Arabidopsis. Plant Cell *12*, 2409–2424. https://doi.org/10.1105/tpc.12.12.2409.

45. Reiter, W.D., Chapple, C., and Somerville, C.R. (1997). Mutants of Arabidopsis thaliana with altered cell wall polysaccharide composition. Plant J. *12*, 335–345. https://doi.org/10.1046/j.1365-313x.1997.12020335.x.

46. Zhao, C., Zayed, O., Zeng, F., Liu, C., Zhang, L., Zhu, P., Hsu, C.C., Tuncil, Y.E., Tao, W.A., Carpita, N.C., et al. (2019). Arabinose biosynthesis is critical for salt stress tolerance in Arabidopsis. New Phytol. *224*, 274–290. https://doi.org/10.1111/nph.15867.

47. Roycewicz, P.S., and Malamy, J.E. (2014). Cell wall properties play an important role in the emergence of lateral root primordia from the parent root. J. Exp. Bot. *65*, 2057–2069. https://doi.org/10.1093/jxb/eru056.

48. Draeger, C., Ndinyanka Fabrice, T., Gineau, E., Mouille, G., Kuhn, B.M., Moller, I., Abdou, M.T., Frey, B., Pauly, M., Bacic, A., et al. (2015). Arabidopsis leucine-rich repeat extensin (LRX) proteins modify cell wall composition and influence plant growth. BMC Plant Biol. *15*, 155. https://doi.org/10.1186/s12870-015-0548-8.

49. Xu, S.L., Rahman, A., Baskin, T.I., and Kieber, J.J. (2008). Two leucine-rich repeat receptor kinases mediate signaling, linking cell wall biosynthesis and ACC synthase in Arabidopsis. Plant Cell *20*, 3065–3079. https://doi.org/10.1105/tpc.108.063354.

50. Escobar-Restrepo, J.M., Huck, N., Kessler, S., Gagliardini, V., Gheyselinck, J., Yang, W.C., and Grossniklaus, U. (2007). The FERONIA receptor-like kinase mediates male-female interactions during pollen tube reception. Science *317*, 656–660. https://doi.org/10.1126/science.1143562.

51. Seifert, G.J. (2021). The FLA4-FEI Pathway: A Unique and Mysterious Signaling Module Related to Cell Wall Structure and Stress Signaling. Genes *12*, 145. https://doi.org/10.3390/genes12020145.

52. Markakis, M.N., De Cnodder, T., Lewandowski, M., Simon, D., Boron, A., Balcerowicz, D., Doubbo, T., Taconnat, L., Renou, J.P., Höfte, H., et al. (2012). Identification of genes involved in the ACC-mediated control of root cell elongation in *Arabidopsis thaliana*. BMC Plant Biol. *12*, 208. https://doi.org/10.1186/1471-2229-12-208.

53. Woeste, K.E., Ye, C., and Kieber, J.J. (1999). Two Arabidopsis mutants that overproduce ethylene are affected in the posttranscriptional regulation of 1-aminocyclopropane-1-carboxylic acid synthase. Plant Physiol. *119*, 521–530. https://doi.org/10.1104/pp.119.2.521.

54. Alonso, J.M., Hirayama, T., Roman, G., Nourizadeh, S., and Ecker, J.R. (1999). EIN2, a bifunctional transducer of ethylene and stress responses in Arabidopsis. Science *284*, 2148–2152. https://doi.org/10.1126/science.284.5423.2148.

55. Granger, C.L., and Cyr, R.J. (2001). Spatiotemporal relationships between growth and microtubule orientation as revealed in living root cells of Arabidopsis thaliana transformed with green-fluorescent-protein gene construct GFP-MBD. Protoplasma *216*, 201–214. https://doi.org/10.1007/BF02673872.

56. Siddique, S., Radakovic, Z.S., De La Torre, C.M., Chronis, D., Novák, O., Ramireddy, E., Holbein, J., Matera, C., Hütten, M., Gutbrod, P., et al. (2015). A parasitic nematode releases cytokinin that controls cell division

and orchestrates feeding site formation in host plants. Proc. Natl. Acad. Sci. USA *112*, 12669–12674. https://doi.org/10.1073/pnas.1503657112.

57. Street, I.H., Aman, S., Zubo, Y., Ramzan, A., Wang, X., Shakeel, S.N., Kieber, J.J., and Schaller, G.E. (2015). Ethylene Inhibits Cell Proliferation of the Arabidopsis Root Meristem. Plant Physiol. *169*, 338–350. https://doi.org/10.1104/pp.15.00415.
58. Smith, A.M. (1976). Ethylene in Soil Biology. Annu. Rev. Phytopathol. *14*, 53–73. https://doi.org/10.1146/annurev.py.14.090176.000413.
59. Sasidharan, R., and Voesenek, L.A.C.J. (2015). Ethylene-Mediated Acclimations to Flooding Stress. Plant Physiol. *169*, 3–12. https://doi.org/10.1104/pp.15.00387.
60. Du, J., Kirui, A., Huang, S., Wang, L., Barnes, W.J., Kiemle, S.N., Zheng, Y., Rui, Y., Ruan, M., Qi, S., et al. (2020). Mutations in the Pectin Methyltransferase QUASIMODO2 Influence Cellulose Biosynthesis and Wall Integrity in Arabidopsis. Plant Cell *32*, 3576–3597.
61. Kuczak, M., and Kurczyńska, E. (2020). Cell wall composition as a marker of the reprogramming of the cell fate on the example of a Daucus carota (L.) hypocotyl in which somatic embryogenesis was induced. Int. J. Mol. Sci. *21*, 8126. https://doi.org/10.3390/ijms21218126.
62. Kohorn, B.D., Greed, B.E., Mouille, G., Verger, S., and Kohorn, S.L. (2021). Effects of Arabidopsis wall associated kinase mutations on ESMERALDA1 and elicitor induced ROS. PLoS One *16*, e0251922. https://doi.org/10.1371/journal.pone.0251922.
63. Ursache, R., Andersen, T.G., Marhavý, P., and Geldner, N. (2018). A protocol for combining fluorescent proteins with histological stains for diverse cell wall components. Plant J. *93*, 399–412. https://doi.org/10.1111/tpj.13784.
64. Majda, M., Grones, P., Sintorn, I.M., Vain, T., Milani, P., Krupinski, P., Zagórska-Marek, B., Viotti, C., Jönsson, H., Mellerowicz, E.J., et al. (2017). Mechanochemical Polarization of Contiguous Cell Walls Shapes Plant Pavement Cells. Dev. Cell *43*, 290–304.e4. https://doi.org/10.1016/j.devcel.2017.10.017.
65. Counsell, A.J., Jones, A.T., Todd, M.H., and Rutledge, P.J. (2016). A direct method for the *N*-tetraalkylation of azamacrocycles. Beilstein J. Org. Chem. *12*, 2457–2461. https://doi.org/10.3762/bjoc.12.239.
66. Francavilla, C., Low, E., Nair, S., Kim, B., Shiau, T.P., Debabov, D., Celeri, C., Alvarez, N., Houchin, A., Xu, P., et al. (2009). Quaternary ammonium N,N-dichloroamines as topical, antimicrobial agents. Bioorg. Med. Chem. Lett. *19*, 2731–2734. https://doi.org/10.1016/j.bmcl.2009.03.120.
67. Lipshutz, B.H., and Taft, B.R. (2006). Heterogeneous copper-in-charcoal-catalyzed click chemistry. Angew. Chem. Int. Ed. Engl. *45*, 8235–8238. https://doi.org/10.1002/anie.200603726.
68. Mosca, G., Eng, R., Adibi, M., Yoshida, S., Lane, B., Bergheim, L., Weber, G., Smith, R.S., and Hay, A. (2023). Growth and tension in explosive fruit. Preprint at bioRxiv. https://doi.org/10.1101/2023.05.15.540759.

## STAR★METHODS

### KEY RESOURCES TABLE

| REAGENT or RESOURCE | SOURCE | IDENTIFIER |
|---|---|---|
| Biological samples | | |
| Arabidopsis thaliana (Col-0) | N/A | N/A |
| Arabidopsis thaliana (WS) | N/A | N/A |
| *mur 1-1* | Reiter et al.[41] | N/A |
| *mur 4-1* | Reiter et al.[41] | N/A |
| *mur 9-1* | Reiter et al.[41] | N/A |
| *mur 11-1* | Reiter et al.[41] | N/A |
| *prc 1-1* | Bouton et al.[40] | N/A |
| *qua 1-1* | Gigli-Bisceglia et al.[37] | N/A |
| *qua2-1* | Gigli-Bisceglia et al.[37] | N/A |
| *gals-10* | Sasidharan and Voesenek[59] | N/A |
| *pXPP>GR>PMEI5* | Fagard et al.[44] | N/A |
| *iPMEIox* | Verger et al.[41] | N/A |
| *pmei5oe* | Wachsman et al.[39] | N/A |
| *the 1-1* | Scheller and Ulvskov[15] | N/A |
| *fer -4* | Zhao et al.[46] | N/A |
| *lrx 3, lrx 4, lrx 5* | Reiter et al.[45] | N/A |
| *fei 1* | Roycewicz and Malamy[46] | N/A |
| *fei 2-2* | Roycewicz and Malamy et al.[46] | N/A |
| *ein 2-1* | Seifert et al.[51] | N/A |
| *ein 3-1* | Escobar-Restrepo et al.[50] | N/A |
| *etr 1-1* | Escobar-Restrepo et al.[50] | N/A |
| *eto 1-1* | Escobar-Restrepo et al.[50] | N/A |
| wakΔ | Kohorn et al.[62] | N/A |
| Chemicals, peptides, and recombinant proteins | | |
| Paraformaldehyde | Sigma-Aldrich | 158127 |
| Glutaraldehyde | Sigma-Aldrich | G5882 |
| LRW resin, medium grade - catalyzed | TAAB essentials for microscopy, England, UK | L012 |
| Abscisic acid | Sigma-Aldrich | A1049 |
| Dexamethasone | Sigma-Aldrich | D4902 |
| B-estradiol | Sigma | E8875 |
| 1-Aminocyclopropanecarboxylic acid | Sigma-Aldrich | A3903 |
| 3-Indoleacetic acid | Sigma-Aldrich | I2886 |
| 6-Benzylaminopurine | Sigma-Aldrich | B3408 |
| Methyl jasmonate | Sigma-Aldrich | 392707 |
| Aminoethoxyvinyl glycine hydrochloride | Merck | 32999 |
| rat-LM19 monoclonal antibody | kerafast | ELD001 |
| rat-LM20 monoclonal antibody | kerafast | ELD003 |
| α-Rat- Fluorescein | ImmunoResearch | 2340652 |
| Fluorescent brightener 28 | MP-Biomedical | 02158067-CF |
| Software and algorithms | | |
| R | https://www.r-project.org/ | N/A |
| Fiji | https://imagej.net/ | N/A |
| Morphographx | https://morphographx.org/ | N/A |

## EXPERIMENTAL MODEL AND STUDY PARTICIPANT DETAILS

### Plant materials

Wild-type and mutant *A. thaliana* strains used in this study were ordered from the Nottingham Arabidopsis Stock Centre or obtained directly from the laboratories previously publishing them.

### Plant growth condition

Arabidopsis Seedlings were plated on half-strength (0.5) Murashige and Skoog (MS) medium (Duchefa) with 1% (w/v) sucrose and 0.8% (w/v) agar (pH 5.7). The seeds were stratified for 2 d at 4°C. Seedlings were grown on vertically oriented plates in growth chambers under a 16-h light/8-h dark photoperiod at 21°C.

## METHOD DETAILS

### Hormonal and drug treatment

Seedlings 5–6 d old were transferred onto solid MS medium with or without the indicated chemicals. The drugs and hormones used were 3-indoleacetic acid (IAA; 0.2 μM), 6-Benzyl aminopurine (BAP; 0.2 μM), Abscisic acid (ABA; 1 μM), 1-amino cyclopropane carboxylic acid (ACC; 1 μM), and methyl jasmonate (MeJA; 1 μM). For the isoxaben assays, the roots were treated with 600 nM for 24 hours. For estradiol treatment, estradiol (Sigma-Aldrich, E8875) was added to the growth medium at a final concentration 10 μM. For DEX induction on plate, DEX (Sigma-Aldrich, D4902) was added to the growth medium in a final concentration of 50 μM. Fluorescent dyes used were as follows: propidium iodide (PI; 10 μg/ml), Calcofluor White (CW; 0.01% p/v).

### Confocal imaging and real-time analysis

For confocal microscopy images, the Leica SP8 confocal laser scanning microscope was used. Pictures were taken with a 40× glycerol immersion objective. Fluorescence signals for GFP (excitation 488 nm, emission 500–530 nm) and PI (excitation 536 nm, emission 617 nm) were detected. YFP Signals were observed with the GFP settings. To image Calcofluor White we used 405-nm excitation and detected it at 425–475 nm). For image analyses, the ImageJ (National Institute of Health, http://rsb.info.nih.gov/ij) was used.

### FLIM imaging and analysis

FLIM images were recorded using a Leica TCS SP8 inverted scanning confocal microscope coupled with a Becker-Hickl SPC830 time-correlated single photon counting (TCSPC) module. Pulsed excitation at 488 nm excitation wavelength, generated by a pulsed white light laser with a repetition rate of 40 MHz, was used. Imaging was performed with a 63× 1.2 NA water immersion objective and images were recorded at 256x256 pixel resolution, at a line scanning speed of 400 Hz. Emission was collected using a spectral window of 50 nm bandwidth centered on 525 nm onto a Leica HyD SMD hybrid photodetector.

### Histochemical staining

Ablated seedlings were incubated in a ClearSee solution and incubated for 3 days. After 3 days, the ClearSee solution was replaced with ClearSee solution combining calcofluor white for 2 h.[63]

### Single-cell laser ablation

For laser cell ablation, 5- or 6-d-old seedlings were placed on chambered cover glasses (Nunc Lab-Tek).[20] For laser ablation, a 2-photon laser was used at 800 nm wavelength in the FRAP mode. The same settings were used for ablation in all the samples, the roots were scanned in 10-, 20-, or 30-min intervals for 10 to 15 h. The number of pericycle cell divisions and their orientations (periclinal vs. transverse/anticlinal) were scored on recordings done for a 15-h period from the moment of ablation. At least 20 individual ablation events were analyzed. To detect cell death of ablated cells, the cells were stained with PI.

### Nematode infection

We used cyst nematodes, *Heterodera schachtii*. The incubation and manipulation of cyst nematodes, *Heterodera schachtii*, was done as described previously.[56] 5- or 6-d-old seedlings were infected, and samples were collected 48 hours after infection.

### Atomic Force Microscopy

AFM indentation experiments were carried out with a NanoWizard 4 XP BioScience (ScanAsyst Air, Bruker, Inc.), that was mounted on an optical macroscope (MacroFluo, Leica). All quantitative measurements in lives root were performed with cantilever biosphere B20-CONT (nanotools). For the live root sections, 5 days roots were embedded in 5% low melting agar and the 100 μm sections were made with a vibratome. All quantitative measurements in resin section were performed using RTESPA-150 Cantilever. The sample was then positioned on an XY-motorized stage and held by a magnetic clamp. Then, the AFM head was mounted on the stage and an approximated positioning with respect to the cantilever was done using the optical macroscope. The elasticity of the sample (demonstrated in the images) was estimated using the Hertz model (Derjaguin, Muller, Toropov modulus). Digestions with cellulase (C1184, Sigma-Aldrich) were done for 10 min at 37 C with a concentration of 0.1 w/v.

### Transmission Electron Microscopy imaging

Images of cross sections of Arabidopsis root were obtained using an electron microscope (JEOL 1230 TEM, accelerating voltage 80 kV, with a Gatan MSC 600CW 2k x 2k CCD camera).

### Resin Embedding and Sectioning

Arabidopsis and tomato primary roots were fixed in ice-cold fixation solution (4% Paraformaldehyde and 0.05% Glutaraldehyde dissolved in 100 mM phosphate buffer, pH 7.2) at 4° C overnight. The samples were washed 3 times for 10 min with 100 mM phosphate buffer and embedded in LRW resin, medium grade – catalyzed (TAAB essentials for microscopy, England, UK).[64] Serial cross semi-thin sections (thickness of 500 nm) were prepared using a microtome (HistoCore NANOCUT R, Leica BioSystem).

### Tissue embedding and sectioning for immuno localization

7-day old seedlings of *Arabidopsis thaliana* Col-0 and *qua1.1* lines were fixed in fixation buffer (4% paraformaldehyde (PFA; dissolved in warm dd$H_2O$ supplemented with 2 drops of 0.1 N KOH) for 1h at RT. Roots were separated from the seedlings using a razor blade and washed three times with wash buffer (100mM piperazine-N,N′-bis (2-ethane sulfonic acid) (PIPES) pH 6.8, 1 mM Ethylene glycol tetraacetic acid (EGTA), 1 mM $MgSO_4$). Next, roots were dehydrated progressively (10% increasing concentration) in 100% ethanol and then embedded progressively (10% increasing concentration) in 100% LR white resin (TAAB essentials for microscopy, England, UK) at 55°C for 48h. Sections (1um) were performed using a microtome (HistoCore NANOCUT R, Leica BioSystem).

### Immunocytochemistry

Sections in MilliQ water were fixed on polylisine slides on a hot plate (37°C). Epitope blocking was done for 30 min at RT using 2% (w/v) BSA/Phosphate-buffered saline/0.01% (v/v) Tween-20 (PBST) buffer. Next, sections were incubated in primary antibodies (rat-LM19 monoclonal antibody detecting un-esterified homogalacturonan, Kerafast, ELD001; rat-LM20 monoclonal antibody detecting esterified homogalacturonan, Kerafast, ELD003) diluted 1:50 in PBS supplemented with 2% (w/v) BSA, overnight at 4°C. Then, sections were washed three times with PBST buffer and incubated in α-Rat- Fluorescein (FITC) secondary antibody (Jackson-ImmunoResearch, AB_2340652), diluted 1:1000 in PBS supplemented with 2% (w/v) BSA, overnight at 4°C. Lastly, sections were washed again three times with PBST buffer and mounted in Vectashield vibrance (Vector Laboratories, H-1700-2) mounting medium. The fluorescent images were acquired using the Leica SP8 inverted confocal microscope, with a 40x objective, oil immersion (N.A.=1.3; reflective index n20/D 1.516), pinhole adjusted to 1 Airy Unit. The excitation wavelength was 488 nm (Emission 506nm - 544nm) for the FITC detection.

### Raman Microscopy

Five days old seedlings were used for the Raman assay. The samples' roots were placed on a metallic stainless-steel slide without cover slip, directly under the microscope. Micro-Raman measurements were performed with a modified LabRAM HR Raman confocal microscope (HORIBA Scientific in Kyoto, Japan). A solid-state laser module with a maximum output power of 90 mW, and a central wavelength of 532 nm was responsible for the Raman excitation. Raman signals were recorded with a 50x microscopic objective lens (Olympus LMPlanFL N) that had a NA=0.5 and a working distance of 10.6 mm. The laser power measured on the sample was 30mW with a laser spot size of 1.7 μm in the lateral, and 2 μm in the axial direction. The Raman spectral resolution was around 2 $cm^{-1}$, achieved with a 600-groove grating. The acquisition Raman spectral range was set between 400 and 3,500 $cm^{-1}$, covered with two optical scan windows. In each measurement point, we used an exposure time of 20 seconds, and with two accumulations. Analysis of Raman measurements was performed with LabSpec Software (HORIBA Scientific in Kyoto, Japan).

### Mechano-probe synthesis

#### *Plasma membrane mechanoprobe*

The chemical structure and synthetic route for the plasma membrane mechanoprobe was described previously in Michels et al.[27]

#### *CW mechanoprobe*

A new version of the CW mechanoprobe reported previously[26] was used in this study, in which the original peptide targeting group for CW binding was replaced by a small molecule organic motif that targets the CW. The synthesis of this probe, and its individual steps, is described below.

*Step 1: 4-(azidomethyl)benzaldehyde*

4-(bromomethyl)benzaldehyde (5g, 25 mmol) was added to 50 mL of DMF. $NaN_3$ (2.5 g, 38 mmol) was added, the solution is heated up to 60 ºC and left stirring for 1.5 hours. 250 mL of ethyl acetate was added followed by 250 mL of water. The organic phase was

isolated and washed with 2x250 mL water. The organic phase was dried with $MgSO_4$, concentrated and dried under vacuum to yield 4-(azidomethyl)benzaldehyde as a clear liquid (3.76 g, 93% yield).

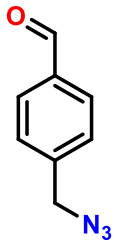


1H NMR (400 MHz, CDCl3) δ 10.02 (s, 1H), 7.90 (d, J = 8.1 Hz, 2H), 7.49 (d, J = 8.5 Hz, 2H), 4.45 (s, 2H).

*Step 2: $N_3$-BODIPY mechanoprobe*

2-methylpyrrole (2.092 mL, 24.82 mmol) and 4-(azidomethyl)benzaldehyde (2.0 g, 12.41mmol) were added to 500 mL anhydrous dichloromethane in a 1L 3-neck round bottom flask equipped with a stirring bar. The solution was sparged with $N_2$ for 30 minutes. Trifluoroacetic acid (500 μL, 6.2 mmol) was added and the mixture was left stirring for 2 hours. 2,3-Dichloro-5,6-dicyano-1,4-benzoquinone (2.82 g, 12.41 mmol) was added after which the mixture was sparged with $N_2$ for 10 minutes followed by 20 minutes of stirring. Di-isopropylethylamine (15.1 mL, 86.7 mmol) was added followed by the addition of boron trifluoride diethyl etherate (15.3 mL, 124 mmol). The reaction mixture was left stirring for 24 hours under and $N_2$ atmosphere. A small amount of 2:3 hexane:ethyl acetate is added to the mixture. Dichloromethane was evaporated under reduced pressure. The product is isolated after purification on silica (2:3 hexane:ethyl acetate) as orange/red crystals (1.07 g, 25% yield).

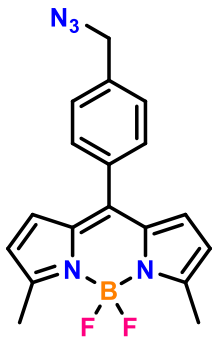


1H NMR (400 MHz, CDCl3) δ 7.52 (d, J = 8.1 Hz, 2H), 7.43 (d, J = 8.1 Hz, 2H), 6.69 (d, J = 4.1 Hz, 2H), 6.27 (d, J = 4.1 Hz, 2H), 4.46 (s, 2H), 2.65 (s, 6H).

*Step 3: 1,4,8,11-Tetra(prop-2-yn-1-yl)-1,4,8,11-tetraazacyclotetradecane*

1,4,8,11-tetraazacyclotetradecane (500 mg, 2.49 mmol) was added to 5 mL of 1M NaOH. 5 mL of acetonitrile was added followed by 1.1 mL of propargyl bromide solution (80% in toluene, 10.2 mmol). The mixture was left stirring overnight after which the precipitate was collected, washed with hexanes an dried to isolate the product (236 mg, 27% yield).

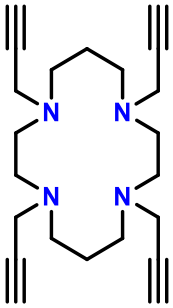


1H NMR (400 MHz, CDCl3) δ 3.44 (s, 8H), 2.62 (s, 16H), 2.17 (s, 4H), 1.77 (s, 4H), 1.61 (s, 4H).

Based on: https://www.beilstein-journals.org/bjoc/articles/12/239[65]

*Step 4: (2-azidoethyl)trimethylammonium bromide*

$NaN_3$ (0.65 g, 10.1 mmol) and (2-bromoethyl)trimethylammonium bromide (1 g, 4.05 mmol) were added to 30 ml of DMF. The mixture is left stirring overnight and then partially concentrated. THF was added after which the white precipitate was isolated and dried to yield (2-azidoethyl)trimethylammonium bromide (480 mg, 57% yield).

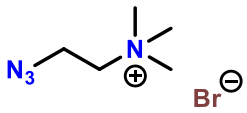

1H NMR (400 MHz, D2O) δ 4.01 (s, 2H), 3.69 – 3.60 (m, 2H), 3.25 (s, 9H).

Based on: https://www.sciencedirect.com/science/article/pii/S0960894X0900451X?via%3Dihub[66]

*Final CW mechanoprobe*

$N_3$-BODIPY (60 mg, 0.17 mmol), 1,4,8,11-Tetra(prop-2-yn-1-yl)-1,4,8,11-tetraazacyclotetradecane (60 mg, 0.17 mg) and Cu impregnated activated charcoal prepared following the procedure by Lipshutz and Taft (https://onlinelibrary.wiley.com/doi/10.1002/anie.200603726)[67] (17 mg) were added to 0.4 mL 1,4-dioxane in a 0.5 mL microwave vial. The mixture was heated in a Biotage initiator+ system under continuous stirring at 150 ºC stirring for 20 minutes. The mixture was filtered (celite) and dried. From this product 39 mg was added to a 0.5 mL microwave vial followed by (2-azidoethyl)trimethylammonium bromide (87 mg, 0.42 mmol) and Cu impregnated activated charcoal (17 mg). Finally 0.25 mL MilliQ water and 0.25 mL 1,4-dioxane were added and the mixture was heated in a Biotage initiator+ system under continuous stirring at 150 ºC for 20 minutes. The resulting product was run over a 0.5 g silica C18 SPE column. 6.6 mg of product was isolated as red crystals and used without any additional purification.

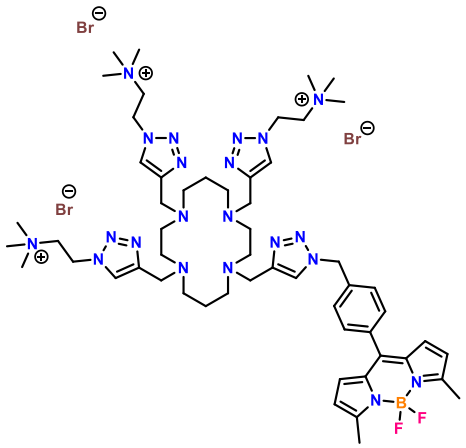

## Model and Finite Element Model

A 3D cellular model was created to represent root structure, starting from a 2D cell outline obtained from a root confocal image. The 2D cross section was converted into a 3D cylindrical structure using the extrusion function of CellMaker, which is a part of the MorphoDynamX software suite (www.MorphoDynamX.org). The model was organized into five distinct layers: the epidermis, cortex, endodermis, pericycle, and stele, with cell lengths of 150 μm, 200 μm, 120 μm, 100 μm, and 200 μm, respectively. To resemble the natural arrangement of cells in a root, the cells in the model were arranged in a staggered pattern in the longitudinal direction, both within layers and between adjacent cells. The cells were then triangulated, resulting in a mesh composed of triangles with a surface area close to 10 μm2 each. This 3D model closely resembled a real root structure, facilitating the study of root dynamics under various cellular conditions.

The inflation analysis was performed employing the Finite Element Method (FEM), using the MorphoMechanX software, an extension of the MorphoDynamX suite developed for finite element mechanical simulations. See Mosca et al.[68] for a detailed description of the framework. Triangular membrane elements with an isotropic St. Venant material were used, with the thickness set to 1μm, the Young's modulus set to 50 MPa and a Poisson's ratio set to 0.3. The turgor pressure was set to 0.5 MPa for all cells.

Two distinct modelling scenarios were implemented. The first scenario used a uniform stiffness across all cellular layers, whereas the second one incorporated a differential stiffness profile, with the stiffness of the epidermal layer and the endodermis-cortex layers being ten times higher than that in the uniformly stiff model. Within each of these scenarios, three cases of cellular ablation were considered: no ablation, ablation of an endodermal cell, ablation of a cortex cell, or ablation of a pericycle cell. Ablation was performed by removing the ablated cell from the simulation and reapplying the boundary conditions (pressure).

In the simulation of ablation dynamics, the pressure was first increased to 1MPa to simulate the initial expansion after heating, and then dropped to 0MPa to represent an ablated cell with no pressure.

Links to the model and the simulation software

https://drive.google.com/file/d/1pCw5nNCGZ5TV211tABHIZ28JOwmoMRBo/view?usp=sharing
https://drive.google.com/file/d/1xRIbMG5KK5x86bRbm9Bq9Hcc5EbY6bKc/view?usp=sharing

## QUANTIFICATION AND STATISTICAL ANALYSIS

Pericycles cell shrink were measured using ImageJ.

Atomic Force microscopy data was analyzed using JPK NanoWizard SPM software version 6.0.

For root stained with mechano-probes, after image acquisition, SPCImage 8.5 software (Becker & Hickl) was used to select and bin ROIs and quantified the data. A two-component exponential decay was used to determine the average fluorescence lifetimes.

Quantification data are analyzed by using R-studio (https://posit.co/download/rstudio-desktop/). All statistical analyses were performed with either Wilcoxon paired test or One-Way ANOVA (Tukey's multiple comparisons test). Statistical details as value of n for each measurement, the p value and the definition of significance are all presented in the figure legends and figures.